

Application of Wavelet Transform to Meteosat-Derived Cold Cloud Index Data over South America

SRINIVASA RAO CHAPA, VADLAMUDI BRAHMANANDA RAO, AND GANNABATHULA SRI SESHA DURGA PRASAD

Instituto Nacional de Pesquisa Espaciais, São José dos Campos, Sao Paulo, Brazil

(Manuscript received 31 March 1997, in final form 22 July 1997)

ABSTRACT

Cold cloud index (CCI) data derived from Meteosat infrared imagery are used to detect periodicities in convective activity in South America. The generally used Fourier transform (FT) cannot provide time-localized information but gives information on the average periodicity of oscillations over the entire time domain. As many events in the atmosphere are intermittent, wavelet transform (WT) is used to identify periodic events in CCI data.

First, the Morlet WT is applied to different combinations of time series data of known periodicities to demonstrate the advantage of WT over FT. Later it is applied to CCI data over four 9° square areas between the latitudes 4.5°N and 31.5°S , and longitudes 54° – 45°W . Near the equator periodic convective activities are observed to be more prominent in the boreal summer than in the austral summer. Between the latitudes 4.5° and 22.5°S , 1-, 2–3-, approximately 5-, and 8–10-day oscillations are seen in the austral summer and seldom is any convective activity seen in the winter. In January semidiurnal variation of cloudiness is also observed for a few days. Farther south in the extratropics, approximately 10- and approximately 20-day periodic events, which refer to the baroclinic waves, are seen more prominently in the austral autumn and winter, and 1- and approximately 5-day oscillations are seen in the summer, perhaps due to convective cloudiness.

1. Introduction

Studies have been made over at least the last 50 years to identify periodic events in the atmosphere, and are useful as forecasting guides by themselves or in conjunction with numerical models. In the Tropics, cumulus clouds, which are the major energy sources for atmospheric circulation, are often associated with systems such as cloud clusters, super cloud clusters, or wave disturbances (Lau et al. 1989, 1991). These organized convective systems vary with different timescales ranging from a few hours to several months. Among these timescales of tropical convection, diurnal, synoptic, intraseasonal, and seasonal variations are more prominent. As a major part of South America lies in the Tropics, we are interested in identifying periodic events in convective activity in South America in terms of Meteosat-derived cold cloud index (CCI).

CCI is defined as the number of pixels colder than 243 K (-30°C) in an area. The threshold temperature 243 K generally corresponds to the mean air temperature around 400 hPa, and thus, CCI represents an index for deep convective clouds whose top exceeds 400 hPa. Many studies have shown that when sufficiently large

areas are considered there are high correlations between the areal extent of cold clouds and areal-average rainfall. Arkin (1979) found high correlations for all the thresholds between 225 and 255 K. As warmer clouds below 400 hPa (>245 K) include nonraining clouds, and colder clouds (<235 K) exclude even a few raining clouds, a threshold temperature of 243 K is considered in the present study. Higher values of CCI indicate more cold clouds and strong convection in that area.

Among the various timescales of tropical convection, diurnal and annual cycles are more prominent. The diurnal cycle of tropical cloudiness may be due to the interaction between the local and large-scale environmental circulations. The diurnal cycle in tropical cloudiness has been studied by many investigators (Murakami 1983; Gray and Jacobson 1977; Nitta and Sekine 1994) and it was found to be more prominent over regions with intense convection.

By applying harmonic analysis to three-hourly geostationary infrared (IR) data, Meisner and Arkin (1987) and Chapa and Rao (1997) found that during the summer, spatially consistent maximum cloudiness was observed in the tropical areas of South America around 1700–1800 local time (LST), and a second maximum was observed around 0900–1100 LST. The second maximum in cloudiness suggests the existence of semidiurnal variations in addition to diurnal variations in convection. The semidiurnal variations in convective activity could be due to atmospheric solar tide oscillation

Corresponding author address: Dr. Srinivasa Rao Chapa, INPE, 12201-970 São José dos Campos, SP, Brazil.
E-mail: chapa@met.inpe.br

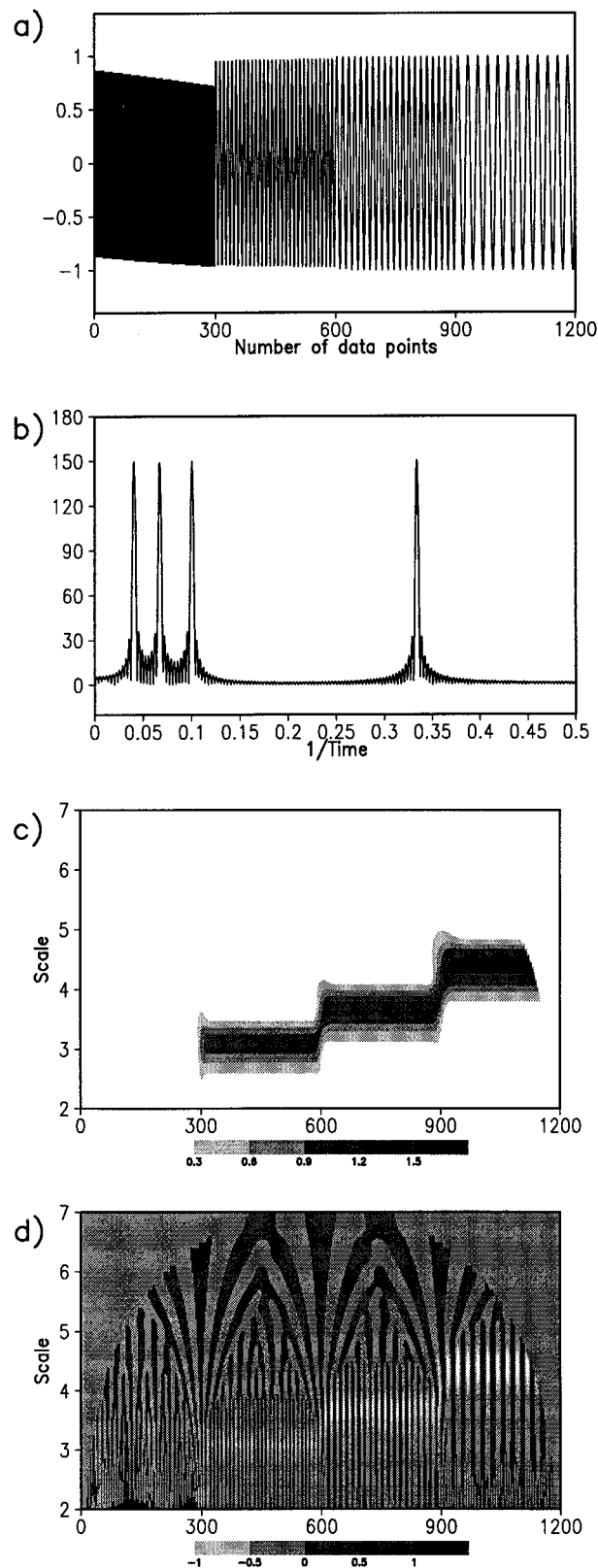


FIG. 1. (a) Time series of four different frequencies padded together, (b) their Fourier spectral magnitudes, (c) their corresponding moduli, and (d) real component of the wavelet coefficients.

and the harmonic resonance of the diurnal forcing (Brier and Simpson 1969).

The other prominent variations observed in the Tropics are intraseasonal oscillations (Madden and Julian 1971). Many investigators, such as Yasunari (1980), Nakazawa (1988), and others, have reported that the intraseasonal oscillations are accompanied by large-scale convective activity that propagates eastward from the Indian Ocean into the western Pacific. Nakazawa (1988) used three-hourly geostationary outgoing long-wave radiation (OLR) data and found that the eastward-moving cloud systems are confined to within 15° of the equator and thereafter the movement on all spatial scales tends to be westward. Knutson and Weickmann (1987) and Hsu et al. (1990) have reported eastwardly propagating signals in the western Pacific, central Africa, and South America, where active convection persists. They also observed strong standing oscillations in these areas, which play an important role in the evolution of intraseasonal oscillations there. Kousky (1988) used pentad OLR data and found intraseasonal variations over South America. Hsu et al. (1990), Ghil and Mo (1991), Hsu (1996), and others reported the existence of intraseasonal oscillations in the extratropics.

Nakazawa (1988) suggested the presence of organized high-frequency structures embedded in tropical intraseasonal oscillations over the tropical western Pacific. The high-frequency oscillations are governed by interactions among intraseasonal oscillations, synoptic-scale disturbances, and organized deep convection. Lau et al. (1991) and Weng and Lau (1994) have suggested that the interaction of diurnal and annual variations with self-excited oscillations in the tropical atmosphere may generate mixed oscillations like synoptic and intraseasonal oscillations. The high-frequency convective systems exist for a season or two in a year, but they may be related to the occurrence of lower-frequency oscillations. Using wavelet analysis, which can demonstrate the time–frequency localization of events, the existence of all such oscillations in the atmosphere in terms of cold cloudiness can be verified.

Fourier transform (FT) is a commonly used technique to study the periodicities of geophysical time series. In Fourier analysis the field is assumed to be homogeneous, and it gives information of average periodicities of the signals over the entire time domain. However, in wavelet analysis the coefficients are displayed in time–frequency frames for the entire time domain at several different timescales separating large-scale behavior from small-scale behavior (Kumar and Foufoula-Georgiou 1993a). The temporal localization of wavelet coefficients displayed in the time–frequency frames is an additional advantage of wavelet transform (WT) over FT. Since some of the meteorological phenomena, such as intraseasonal oscillations, are localized in time, WT is highly suitable to study these phenomena.

In the present study, we first use continuous WT to analyze time series data of known periodicities. Then,

time series of real-valued three-hour-interval CCI data derived from *Meteosat* infrared imagery for one year are analyzed.

2. Study area and data

The data used in the present study are CCI derived from *Meteosat* IR imagery of 3-h interval. For the period November 1994 to May 1995 *Meteosat-3* data are available over the region 4.5°N–40.5°S, 81°–36°W. For the period November 1994 to October 1995 the combined data of *Meteosat-3* and *Meteosat-5* are available over the region 4.5°N–31.5°S, 63°–36°W. The difference in the area coverage is due to the change in the source of satellite data since June 1995. The orbital position of *Meteosat-3* was at 75°W and that of *Meteosat-5* was at 0° over the equator.

In the present study, CCI is derived over 9° × 9° (lat, long) areas in South America between the latitudes 4.5°N–31.5°S, and the longitudes 54°–45°W. As the spatial resolution of a pixel is 5 km × 5 km at the nadir of the satellites, 180 × 180 pixels cover an area near the equator that becomes larger at higher latitudes.

A few days of CCI data are missing in the original dataset. The missing data are for the days 18–28 February (11 days), 1–5 June (5 days) and 18–31 August (14 days) in 1995. Such long gaps would lead to spurious results in the time–frequency distribution of wavelet coefficients, and any kind of interpolation may not produce meaningful data for a few days in sequence. The gaps are filled with zeros. However, wavelet coefficients derived during the periods of gaps should be considered with caution.

3. Method of analysis

a. Introduction to wavelets

Daughter wavelets—or simply wavelets—are functions constructed by dilations and translations of a function that has finite energy (Chui 1992). A continuous nonstationary time series signal can be approximated by daughters of a mother (or an analyzing) wavelet $f(t)$ as follows:

$$F(t) = \alpha^{-1/2} f\left(\frac{t - \beta}{\alpha}\right), \tag{1}$$

where α is a dilation parameter that controls the window width and oscillation period of the base function $f(t)$ within the window [e.g., $f(t) \rightarrow f(\alpha t)$], and β is a translation parameter shifting the window along the time axis [e.g., $f(t) \rightarrow f(t + \beta)$]. Both α and β are real and α is positive.

An admissibility condition for a function $f(t)$ to be an analyzing wavelet is that its Fourier transform $\hat{f}(\omega)$ should satisfy the following criteria:

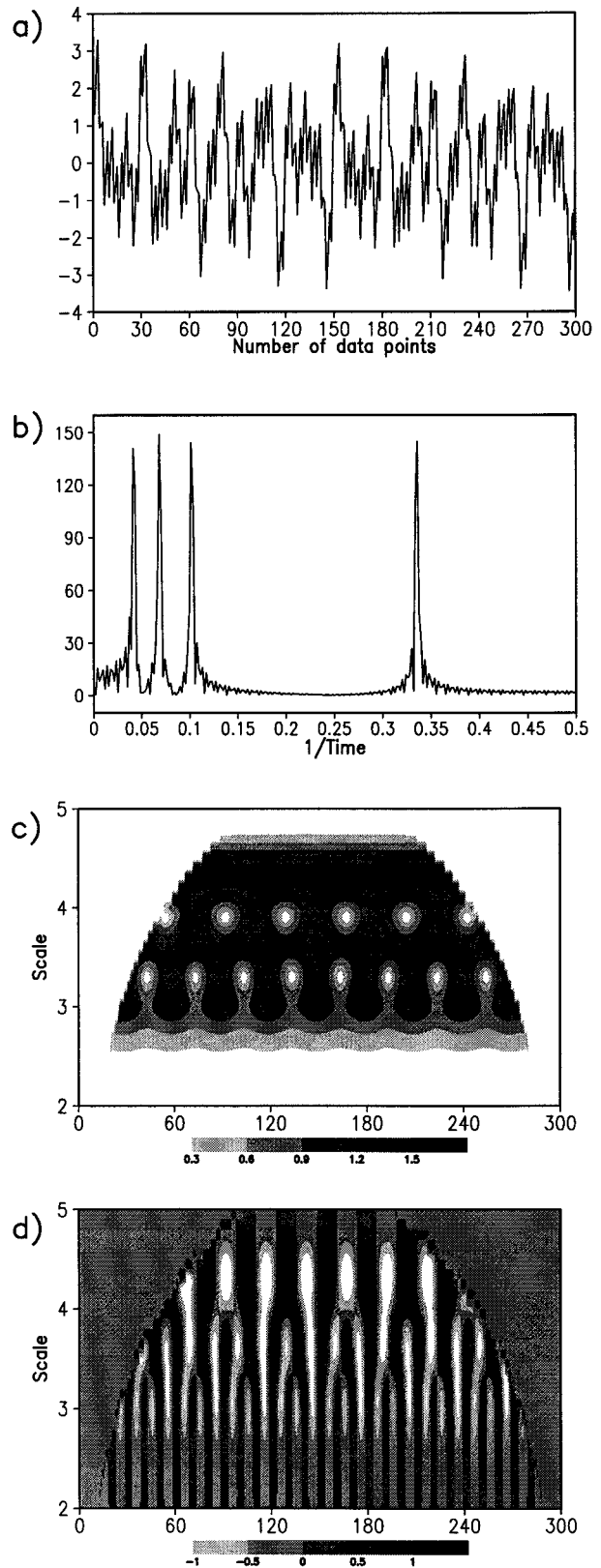


FIG. 2. Same as Fig. 1, but the four time series are overlapped.

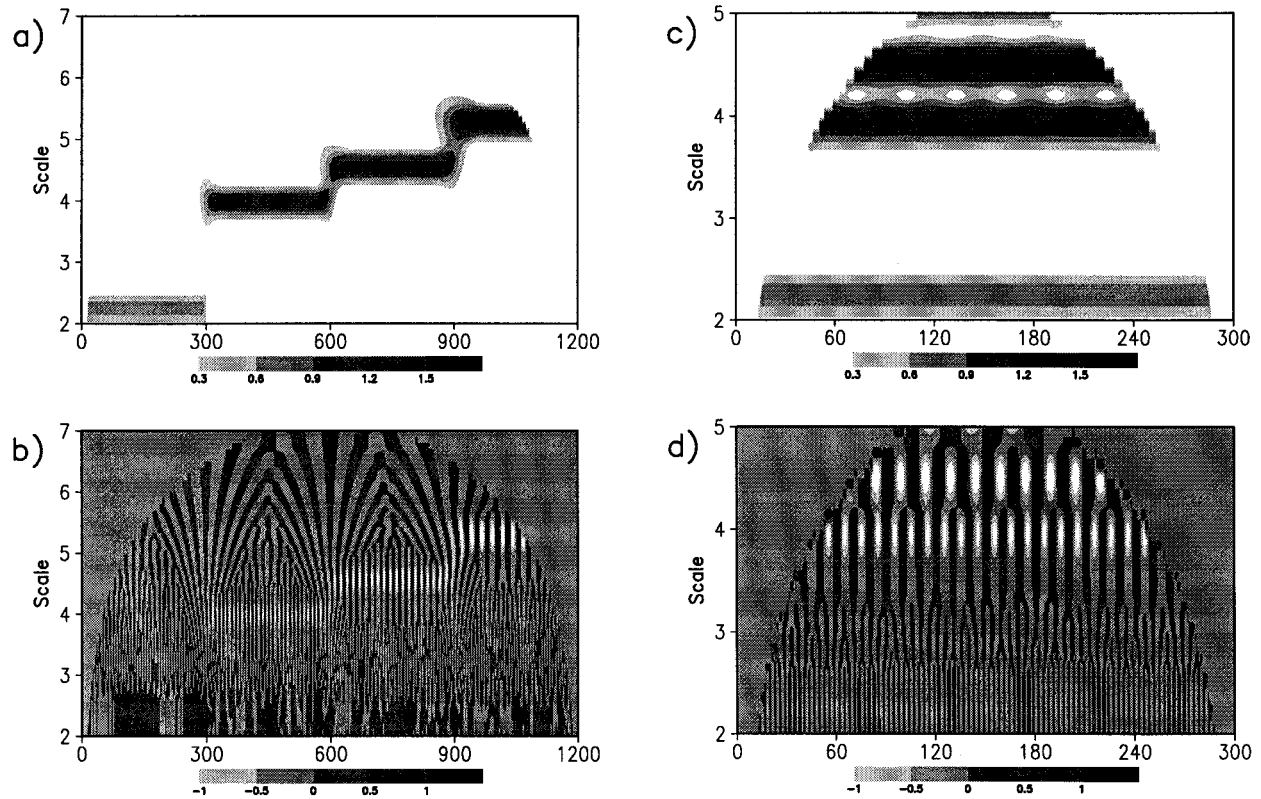


FIG. 3. (a) Moduli and (b) real component of wavelet coefficients for the padded time series data as shown in Fig. 1a for the Morlet wavelet with $\omega_0 = 10.0$. (c) and (d) Same as (a) and (b) but for the overlapped time series data.

$$\int_{-\infty}^{\infty} \frac{|\hat{f}(\omega)|^2}{\omega} d\omega < \infty.$$

In Eq. (1) an energy normalization term, $\alpha^{-1/2}$, is included to ensure that the (daughter) wavelets have the same total energy as the analyzing wavelet. The wavelets have the same shape as that of the analyzing wavelet, and their amplitudes decay sufficiently fast to obtain localization in space or time domain.

Morlet wavelet is a commonly used analyzing wavelet for signal detection in geophysical data. Morlet wavelet is complex and enables one to extract information about the amplitude and phase of the process being analyzed (Grossmann and Morlet 1984). It has the form

$$f(t) = \pi^{-1/4} (e^{-i\omega_0 t} - e^{-\omega_0^2 t/2}) e^{-t^2/2}, \quad (2)$$

which can be approximated as

$$f(t) = \pi^{-1/4} e^{-i\omega_0 t} e^{-t^2/2} \quad (3)$$

for $\omega_0 > 5$, where ω_0 is a wavenumber. For $\omega_0 > 5$, the second term in (2) is neglected, still satisfying the admissibility condition.

Weng and Lau (1994) demonstrated the use of Morlet analyzing wavelet and its daughter wavelets for the varying values of α and β for time series data. They assumed that the value of ω_0 is 5.4.

b. Wavelet transform

A one-dimensional continuous WT was first introduced by Grossman and Morlet (1984). Convolution of a function $g(t)$ with a set of wavelets $F(t)$ derived from the translations and dilations of an analyzing wavelet $f(t)$ is known as wavelet transform. Mathematically it can be expressed as an inner product of $g(t)$ and wavelets $F(t)$, that is,

$$\begin{aligned} Wg(\alpha, \beta) &= \langle g(t)F(t) \rangle \\ &= \int_{-\infty}^{\infty} g(t)F^*(t) dt \end{aligned} \quad (4)$$

$$= \alpha^{-1/2} \int_{-\infty}^{\infty} g(t)f^*\left(\frac{t-\beta}{\alpha}\right) dt. \quad (5)$$

For complex wavelet $F(t)$ we use complex conjugate $F^*(t)$ in the above equations. As mentioned before, $\alpha^{-1/2}$ is used so that $Wg(\alpha, \beta)$ is normalized to unity, where the function g perfectly matches the wavelets F .

Equation (5) expands a one-dimensional time series $f(t)$ into two-dimensional parameter space (α, β) , and yields a local measure of the relative amplitude of activity at scale α and at time β . This is in contrast to the FT that yields an average amplitude over the entire da-

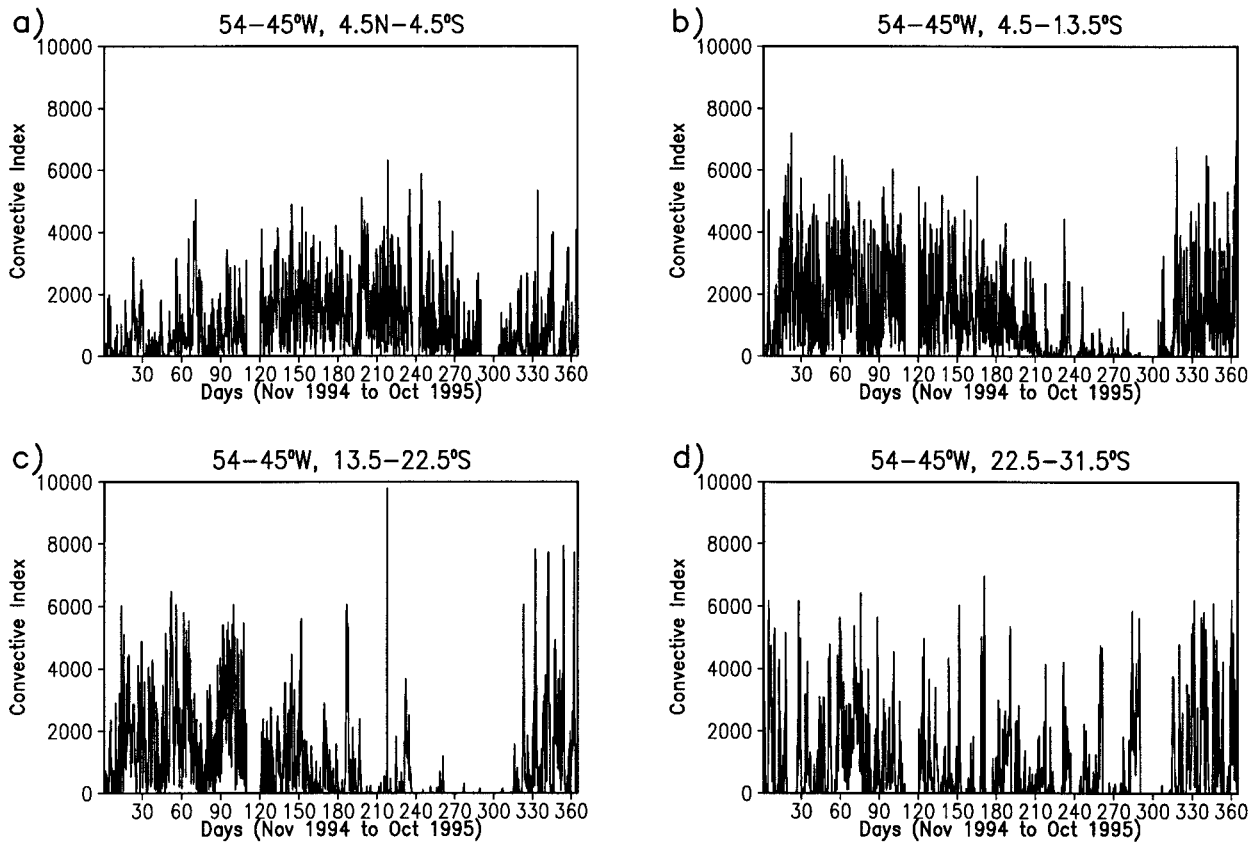


FIG. 4. Time series of cold cloud index over 9° square areas, (a) $4.5^\circ\text{N}-4.5^\circ\text{S}$, (b) $4.5^\circ-13.5^\circ\text{S}$, (c) $13.5^\circ-22.5^\circ\text{S}$, and (d) $22.5^\circ-31.5^\circ\text{S}$, between $54^\circ-45^\circ\text{W}$ based on 3-h data from November 1994 to October 1995.

taset. The WT produces instantaneous coefficients and therefore can yield information on the evolution of non-stationary processes. Recently WT has been applied to time series data in many diversified fields including meteorology (Meyers et al. 1993; Pike 1994; Weng and Lau 1994; Kumar and Foufoula-Georgiou 1993b).

In the case of a Morlet WT, the transform of a Morlet wavelet can be performed either in time domain or in Fourier domain. Since the FT of a Morlet wavelet is a Gaussian function centered at its wavenumber ω_0 , it is easier to perform the Morlet WT in the Fourier domain. The complex Morlet wavelet coefficients can be obtained by taking inner product of FT of the time series data and dilated and translated wavelets expressed in the Fourier domain, and then performing the inverse FT. That is,

$$Wg(\alpha, \beta) = \frac{1}{2\pi} \langle \hat{g}, \hat{F}^* \rangle,$$

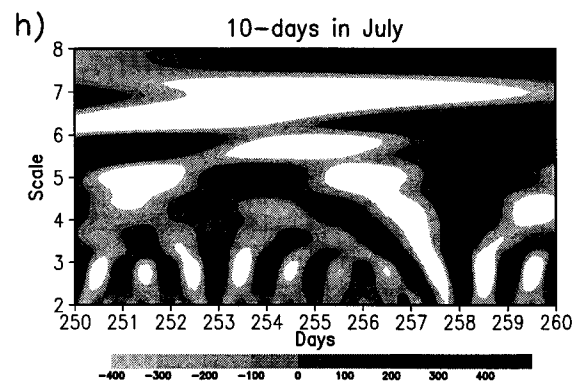
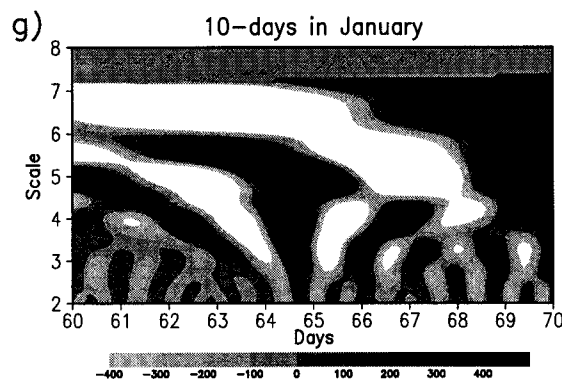
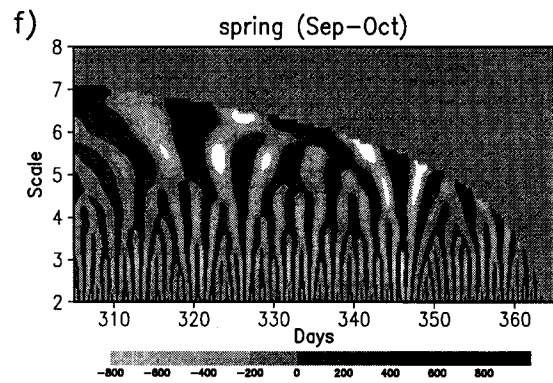
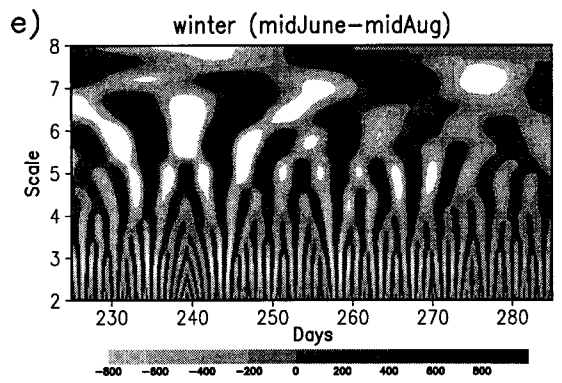
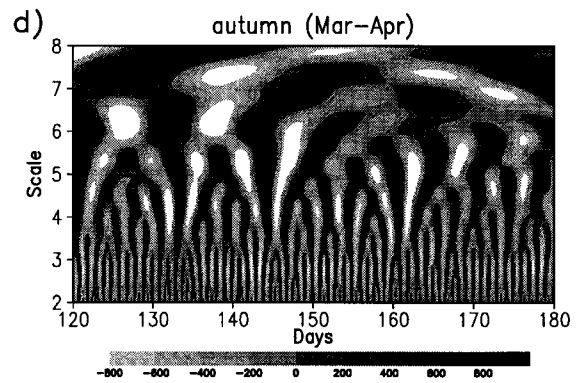
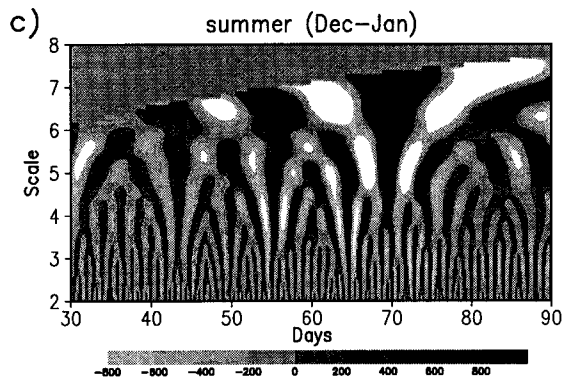
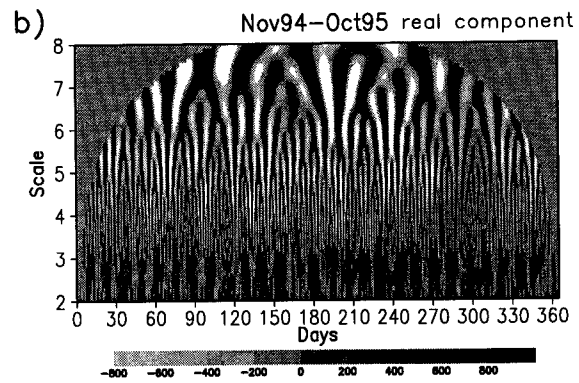
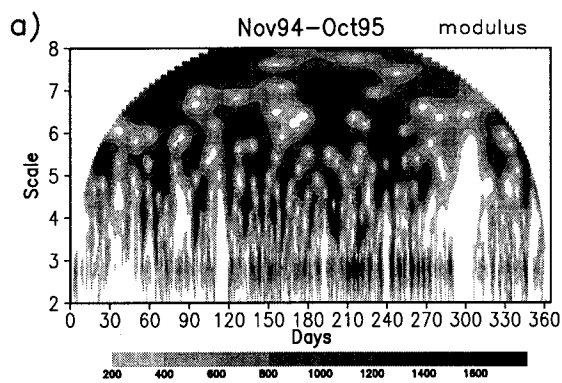
where $\hat{F}(\omega) = \alpha^{1/2} e^{-i\beta\omega} f(\alpha\omega)$. Here the caret denotes FT, and the asterisk denotes the complex conjugate. A complex valued continuous WT provides a modulus, which depicts the intensity, and phase, which detects singularities and measures instantaneous frequencies, whereas real and imaginary parts of the wavelet coefficients depict both the intensity and the phase of the signal variations at particular scales and locations in the time-frequency domain.

4. Application of Morlet transform to artificial datasets

To demonstrate the advantage of WT over FT, using a Morlet analyzing wavelet, WT is applied to two sets of time series of known periodicities. The first set is a padding of four time series of 300 data points, each with the periodicities 3, 10, 15, and 25. The other set is an

FIG. 5. Timescale displays of (a) modulus and (b) real component of Morlet wavelet coefficients ($\omega_0 = 5.3364$) for CCI data over $4.5^\circ\text{N}-4.5^\circ\text{S}$, $63^\circ-54^\circ\text{W}$. (c), (d), (e), and (f) The focused figures on bimonthly domains in each season, summer, autumn, winter, and spring, respectively. (g), (h) The further focused figures on 10-day domains in January and July.

54–45°W, 4.5°N–4.5°S
 $\omega_0 = 5.3364$



overlapping of these four time series on each other. Figures 1a and 2a show how these four time series are combined (note the difference in the number of data points along the abscissa). Figures 1b and 2b show the corresponding spectral magnitudes of Fourier analysis. Abscissa of these figures is time^{-1} , where time corresponds to average periodicities of the time series in the entire time domain. Note that Figs. 1b and 2b look similar, though their input datasets are different.

Figures 1c and 2c present the timescale displays of the modulus, and Figs. 1d and 2d present the real component of the wavelet coefficients ($\omega_0 = 5.3364$) of the datasets shown in Figs. 1a and 2a, respectively. In these figures, scale parameter α is given along the vertical axis (ordinate) and number of data points along the abscissa. The scale at which the wavelet coefficients are calculated is given by

$$\alpha_{m,n} = m + (n/v),$$

where m ($=0, 1, 2, \dots$) is an octave, and n ($=0, 1, \dots, v-1$) is the number of voices per octave, for $v = 10$. The scale is related to the periodicity of the time series signals as

$$\text{period} = \frac{4\pi}{\omega_0 + \sqrt{2 + \omega_0^2}} 2^{\alpha_{m,n}}, \quad (6)$$

where ω_0 is the wavevector as given in the Eq. (5). Similar to the earlier studies by Weng and Lau (1994), ω_0 is considered as 5.3364.

In the figures of modulus and real components of wavelet coefficients (Figs. 1c,d and 2c,d) darker shades correspond to higher values of the coefficients. The real components include the information of phase of the signals in addition to the modulus. In these figures higher values are seen at the scales close to 3.1, 3.7, and 4.4, which correspond to the periods 10, 15, and 25, respectively (see the appendix for the table of relationships between them). In these figures, signals with period 3 are not detected as their corresponding scale is less than 2, at which level the wavelet coefficients are not calculated.

To increase the frequency resolution of the timescale signals, a higher-frequency wavelet ($\omega_0 = 10.0$) is used and the Figs. 1c,d and 2c,d are replotted (Figs. 3a–d). The value of ω_0 should be greater than 5 to neglect the second-order terms in Eq. (4), but satisfy the necessary conditions for the function $f(t)$ to be a Morlet wavelet. By increasing the value of ω_0 to 10.0, the wavelet coefficients are displayed at higher scales than in the case of $\omega_0 = 5.3364$, though the periods of the input signals are unchanged. In Figs. 3a–d signals with period 3 can be found at scale 2.3, and signals with time periods 10, 15, and 25 are found near the scales 4.0, 4.6, and 5.3, respectively. That means resolution of higher frequency signals increases by displaying them at higher scale levels.

Note that the time domain of the WT contains the same number of data points used in the input time series, whereas FT does not give any information about the

number of data points used. By displaying wavelet coefficients in the time domain, the time locality of periodic events can be identified, which is an additional advantage of WT over FT. As all the periodic signals in the padded and overlapped time series are separated out by wavelet analysis, we can infer that wavelet analysis can indeed separate out any periodic event in the atmosphere that is interfered with by other events.

The Morlet WT has an edge effect at the beginning and the end portions of time domain. The timescale displays of the wavelet coefficients are conical in shape, hence much information is lost at the edges of the frames at higher scales. To reduce such an edge effect, Weng and Lau (1994) padded some data points of known periodicity to the original data points prior to computing Morlet WT. Finally, the wavelet coefficients beyond the time domain of the original data are discarded at every scale and the wavelet coefficients of the original data points are kept. However, the padding technique does not calculate the wavelet coefficients at the edges; rather it extrapolates them there by not adding any extra accuracy. Thus, in the present study such padding technique is not used but confined to linear convolution of time series signals with the Morlet wavelet.

5. Application of Morlet WT to cold cloud index data

As we are interested in studying periodicities of convective activities at different latitudes in South America, we have chosen $9^\circ \times 9^\circ$ areas between 4.5°N and 31.5°S . The longitudinal position of these areas is between 54° and 45°W . Figures 4a–d show the time series of CCI over these areas for one year, from November 1994 to October 1995 at 3-h time intervals. As mentioned before, the original time series data have gaps that are filled with zeros. Hence wavelet coefficients during these gap periods should be considered with caution.

Near the equator (Fig. 4a) more cold clouds are observed between days 120 and 270 (March to July) when the intertropical convergence zone (ITCZ) is close to the equator. Figures 4b and 4c show high values of CCI in the tropical areas between 4.5° and 22.5°S in the austral spring and summer than in the other seasons. However, due to frontal effects in the higher latitudes, cold clouds are observed year-long between 22.5° and 31.5°S (Fig. 4d). It is difficult to discern any periodicities from these figures, but some 30–40-day oscillations are apparent in Figs. 4b and 4c. To extract more information of periodicities, the time series data are subjected to the technique of wavelet transform.

Wavelet transform is applied to the real-valued CCI data over the four $9^\circ \times 9^\circ$ areas by using complex Morlet analyzing wavelet [Eq. (3)]. Figure 5a shows the modulus of wavelet coefficients of the CCI data considered over the area 4.5°N – 4.5°S , 54° – 45°W , and Fig. 5b shows the real component. Figures 5c–h present the same real component of the wavelet coefficients shown in Fig. 5b but

54–45°W, 4.5°N–4.5°S
 $\omega_0 = 10.0$

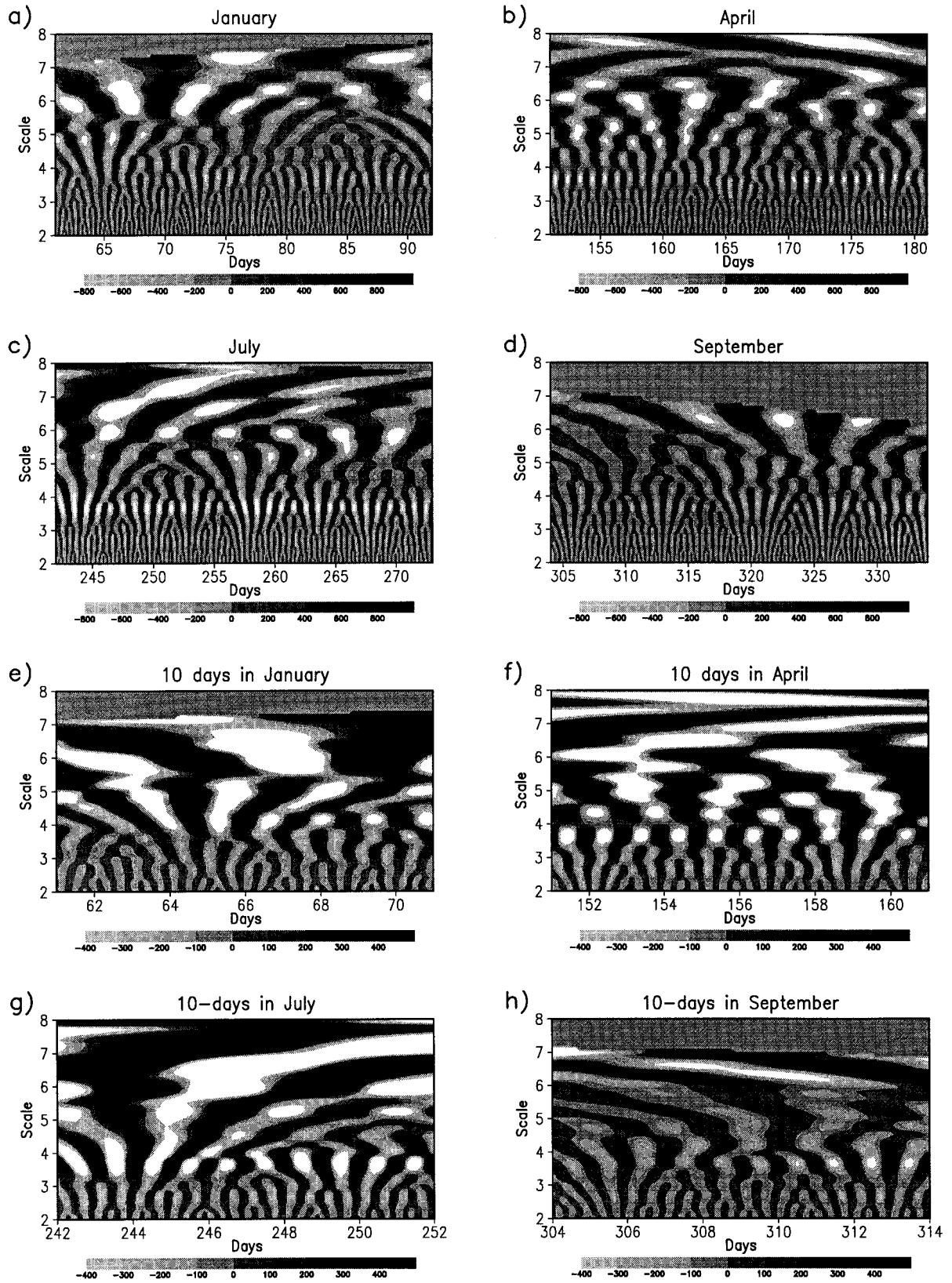


FIG. 6. Timescale displays of real components of Morlet wavelet coefficients with $\omega_0 = 10$ focused on time domains (a) January, (b) April, (c) July, and (d) September. Further focused figures on 10-day domains in (e) January, (f) April, (g) July, and (h) September.

54–45°W, 4.5–13.5°S

$$\omega_0 = 5.3364$$

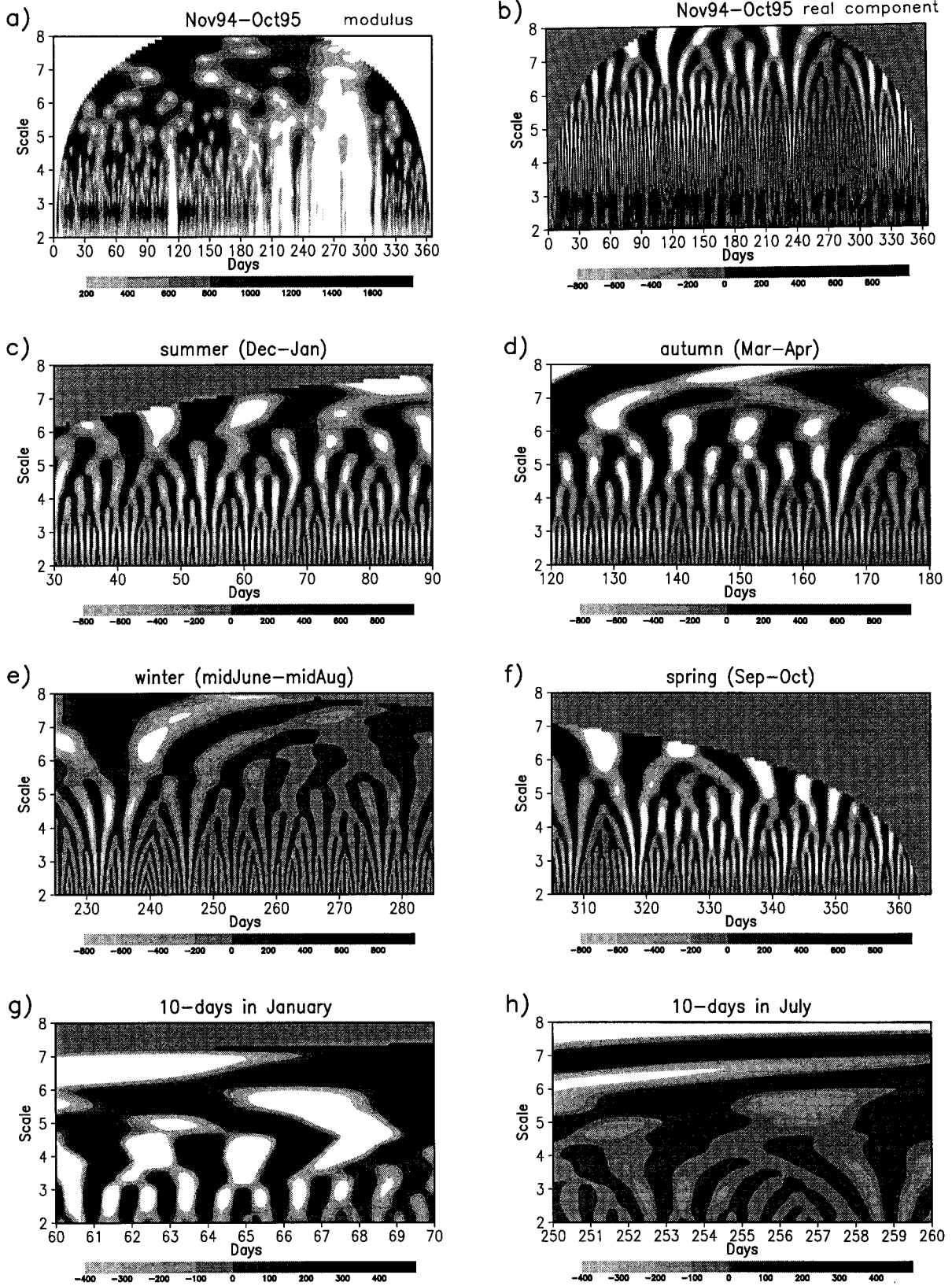


FIG. 7. Same as those in Fig. 5 but over the area 4.5°–13.5°S, 54°–45°W.

54–45°W, 13.5–22.5°S

$\omega_0 = 5.3364$

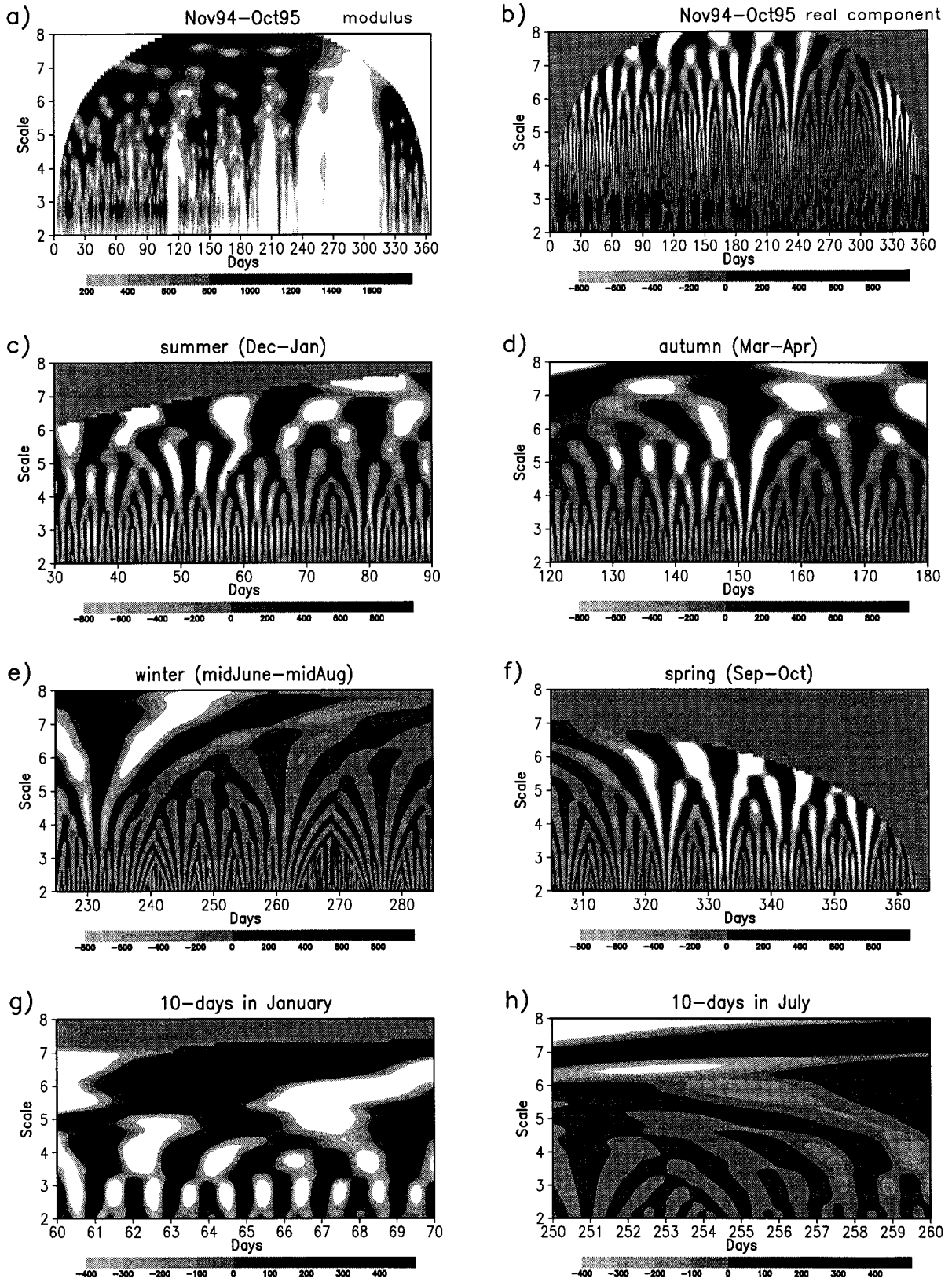


FIG. 8. Same as those in Fig. 5 but over the area 13.5°–22.5°S, 54°–45°W.

54–45°W, 4.5–13.5°S
 $\omega_0 = 10.0$

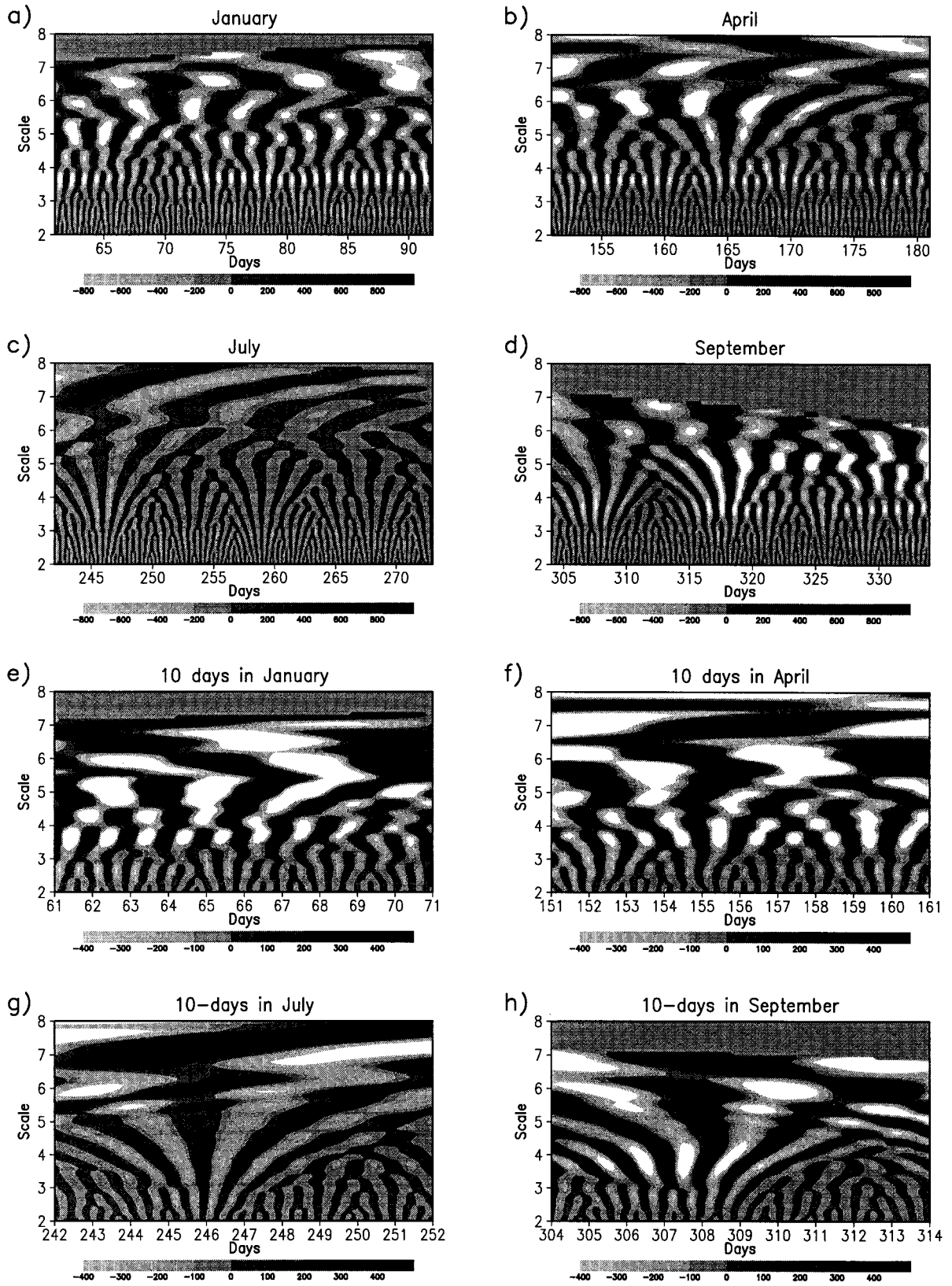


FIG. 9. Same as those in Fig. 6 but over the area 4.5°–13.5°S, 54°–45°W.

54–45°W, 13.5–22.5°S
 $\omega_0 = 10.0$

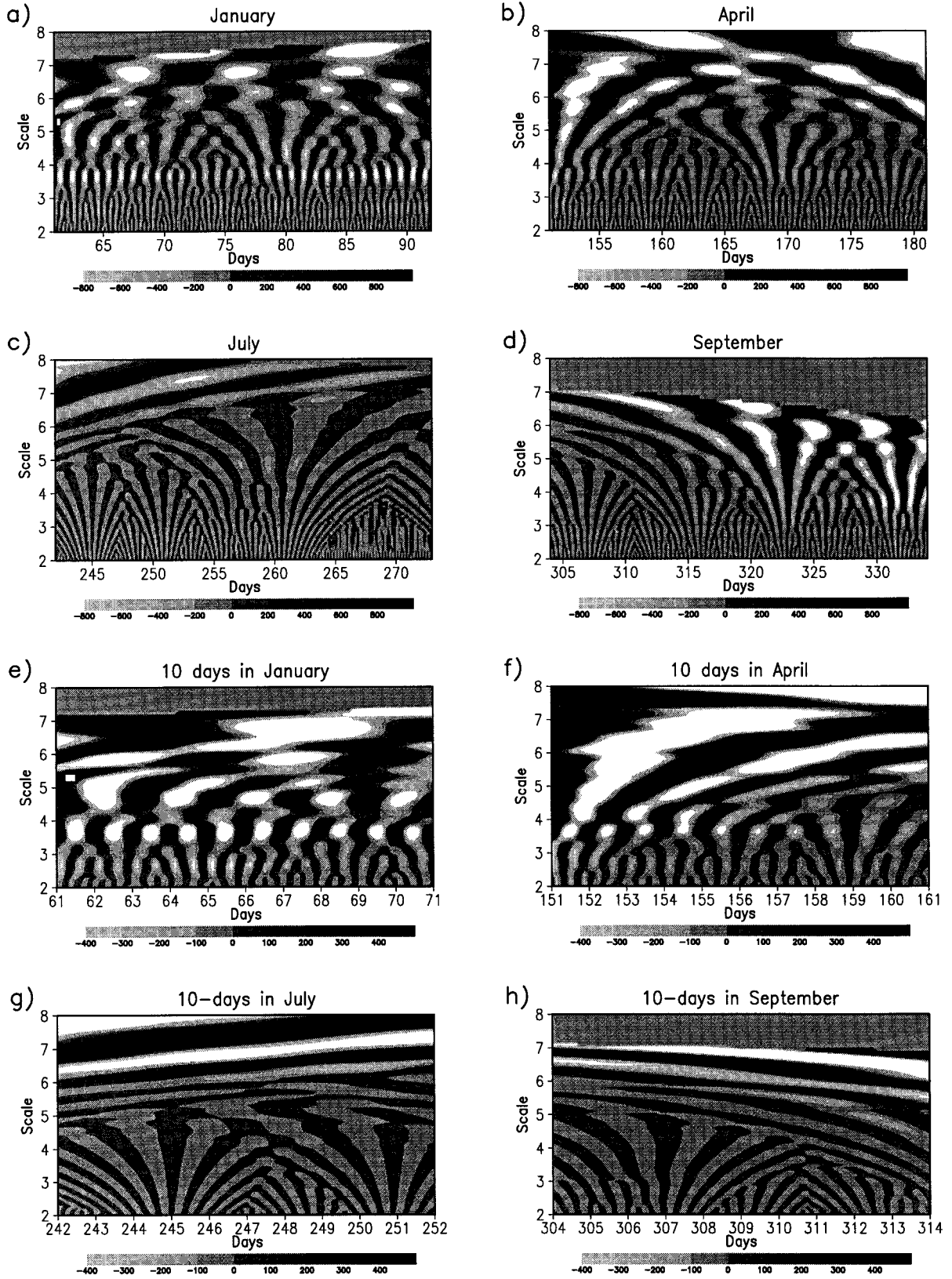
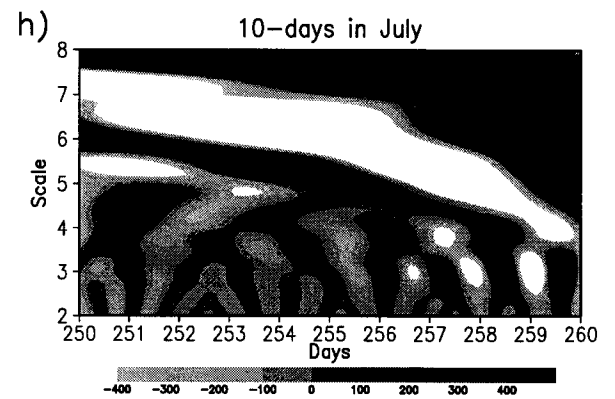
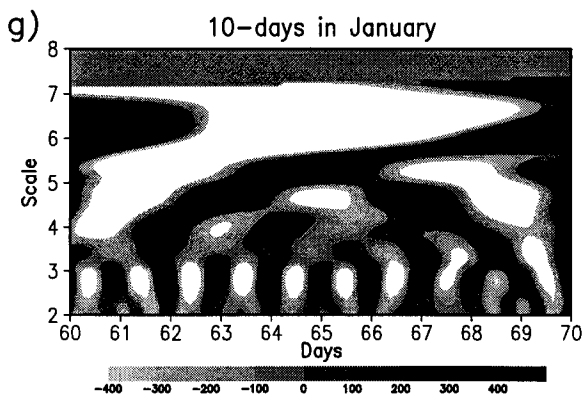
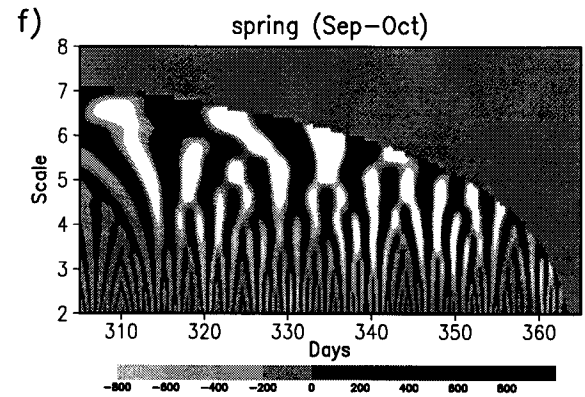
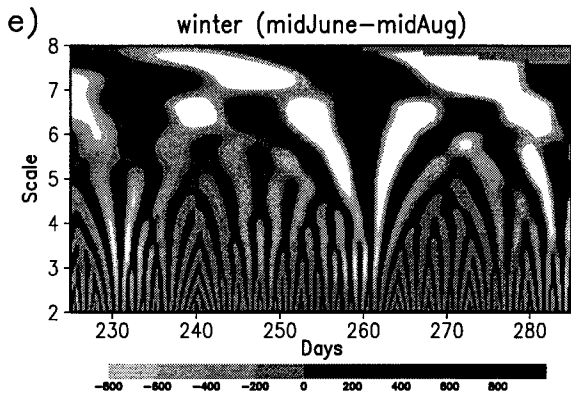
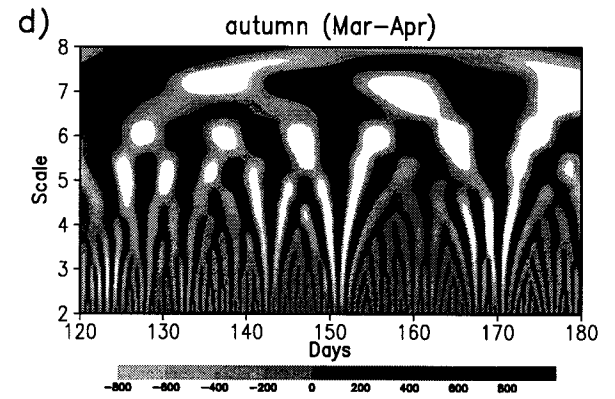
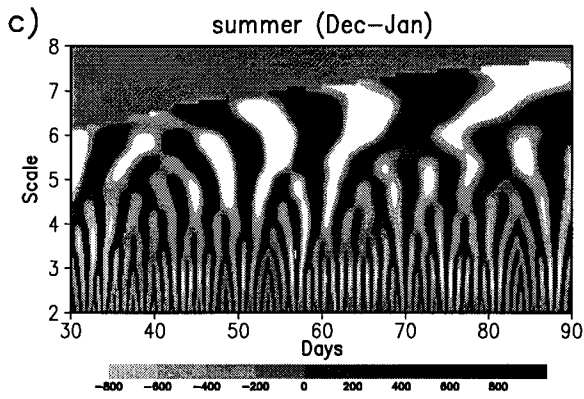
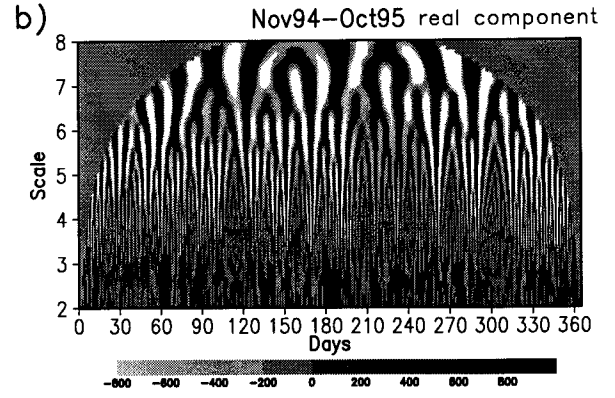
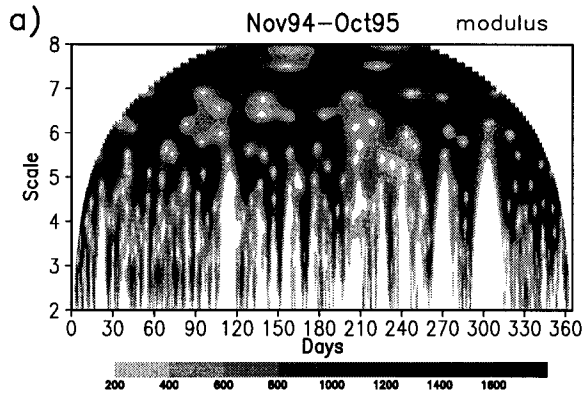


FIG. 10. Same as those in Fig. 6 but over the area 13.5°–22.5°S, 54°–45°W.

54–45°W, 22.5–31.5°S
 $\omega_0 = 5.3364$



focus on individual seasons and even shorter periods. In these timescale displays the abscissa is the time shift over 3 h (but labeled in days), and the ordinate is a scale, that is related to period as shown in Eq. (6) and the appendix.

The modulus depicts intensity of CCI at particular scales and locations, but the real part of the coefficients includes the information of phase as well. Thus, the periodic signals appear better in the frames of the real part of the coefficients than in the modulus frame. In Fig. 5a, high-frequency signals appear between scales 2 and 3 between days 120 and 270 (austral autumn and winter days), similar to those in Fig. 4a. The signals at the same scale levels in Fig. 5b are too close to be identified. As the data period considered is one year, the maximum scale level (scale 8) displayed in the frames refers to the period 296 (~ 37 days) for $\omega_0 = 5.3364$ (see the appendix). To detect intermediate frequency (4–30 days) oscillations more easily, the real component of the wavelet coefficients are plotted on bimonthly time domains (Figs. 5c–f).

In Fig. 5a, higher values of modulus of the wavelet coefficients are seen between days 60 and 270 above the scale 6. At the same scale, regularly spaced maxima and minima are seen in the real component frame (Fig. 5b) during the same period. Periodicity of these oscillations is approximately 20 days. In Fig. 5b more signals appear between scales 5 and 6, particularly in the austral winter (boreal summer). In the bimonthly frames (Fig. 5c–f) mixed signals of periods of about 5 days and 7–8 days are seen in autumn and winter. As it is difficult to discern any periodic signals below the scale 5 from these frames, they are replotted on 10-day time domains (Figs. 5g,h). In these figures diurnal variation of convective cloudiness is more prominent in July (boreal summer) than in January (boreal winter).

For a better resolution in scale, the value of ω_0 is increased to 10.0, such that the wavelet coefficients are displayed at higher scales than in the case of $\omega_0 = 5.3364$ (as discussed in section 4). Figures 6a–d show timescale frames of real components focused on a month in each season. The approximately 5-day and 7–8-day oscillations seen in Fig. 5b–f are better seen in these monthly frames. Note that there is a change in the scale levels, but the periodicities of the signals remain the same (see the appendix). Diurnal and other higher-frequency oscillations are also seen in these frames, but in the frames of 10-day time domains (Figs. 6e–h) the diurnal variations (at the scale 5.7) are more prominent in April and July than in January and September. There are signs of semidiurnal variations (at scale 2.7) as well in April and July, but their magnitudes are quite low.

CCI data are analyzed over the other areas between

4.5° and 22.5°S and 54° and 45°W. Moduli of the wavelet coefficients over the areas 4.5°–13.5°S, 54°–45°W, and 13.5°–22.5°S, 54°–45°W are shown in Figs. 7a and 8a, respectively. It is apparent from these figures that there was not much convective activity in the austral winter (hereafter all seasons refer to the Southern Hemisphere) in these areas. Figures 7b and 8b show the corresponding real components. In these figures approximately 20-day oscillations are apparent (around the scale 7) in the summer and autumn. These signals appear to be hidden in the early summer and late spring due to the edge effects. In the bimonthly frames (Figs. 7c–f and 8c–f) these oscillations appear more clearly in the autumn. In these frames some 10–12-day oscillations (around the scale 6.4) are also seen in the summer and autumn. However, in winter no convective activity is seen at any scale. In the 10-day frames (Figs. 7g,h and 8g,h) diurnal and 2–3-day oscillations are prominent in January and no such signals are found in July.

To detect the other intermediate and high-frequency oscillations in these areas, the real component of the wavelet coefficients are plotted on monthly time domains for $\omega_0 = 10$ (Figs. 9a–d and 10a–d). In January and April, 8–10-day, approximately 5-day, and 2–3-day oscillations (around the scales 6.7–7.0, 6.0, and 5.0, respectively) are seen in both the areas. There is no convective activity in July, but it resumes over these areas by mid- to late September. The 10-day frames (Figs. 9e–h and 10e–h) also show strong diurnal and 2–3-day variations of convective cloudiness in summer, autumn, and spring. It is interesting to note that in January semidiurnal signals are also seen for a few days at the scale 2.7.

Farther south, between 22.5° and 31.5°S, high values of CCI are seen throughout the year, as seen in Fig. 4d (Fig. 11a). The corresponding real component frame (Fig. 11b) shows approximately 20-day oscillations (around the scale 7) in the autumn and winter. At this scale level, as discussed before, wavelet coefficients are hidden in the early summer and late spring. In bimonthly time domain frames for each season (Figs. 11c–f) some approximately 10-day oscillations are also seen. These oscillations are more prominent in the autumn and winter than in the other seasons. However, in the spring and summer approximately 5-day oscillations are more prominent. In the 10-day frames (Figs. 11g,h) the diurnal signals are seen only in January, but not in July, suggesting the convective nature of cloudiness in this area in the summer months.

6. Summary and conclusions

The hierarchy of multiscale oscillations in cold cloud index data revealed by the wavelet analysis ranges from

←

FIG. 11. Same as those in Fig. 5 but over the area 22.5°–31.5°S, 54°–45°W.

semidiurnal, diurnal, to synoptic-scale variations. Among these oscillations, 1-day peaks are the result of the combined effects of diurnal cycle of solar radiation and the local atmospheric circulations. These oscillations are more prominent in the convectively active regions, and they are often modulated to 2–3-day oscillations due to the passage of synoptic disturbances. It is observed that when diurnal variations are pronounced, the synoptic (2–3 day) variations are also active.

Apart from these high frequency oscillations, there exist some mixed or intermediate frequency oscillations (4–30 days) both in the tropical and extratropical areas. These may interact strongly with successive longer scales. These oscillations might be due to the interaction of the dynamic sources causing the independent oscillations such as synoptic and 30–50-day intraseasonal variations, and sun-dependent diurnal and annual variations. The intermediate frequency signals are strong in spring and summer in the tropical areas, and in autumn and winter in the higher latitudes. Near the equator, 7–8-day and approximately 5-day period signals are seen throughout the year, but they are more prominent in the winter (boreal summer).

In the other tropical areas, between 4.5° and 22.5°S, approximately 20-day oscillations are seen in the autumn and winter. They could not be detected in the summer and spring, as the wavelet coefficients are hidden due to the edge effects at the higher scale levels. However, 10–12-day oscillations are observed more prominently only in the summer and autumn. The other high-frequency oscillations like approximately 5-day and 2–3-day are also prominent in the summer and early autumn. During the same period diurnal variations, and for a short period, semidiurnal variations of convective cloudiness are also seen. In the winter and early spring no convective activity is seen at any scale in these areas.

McGuirk and Reiter (1976) have noted the existence of a tropospheric vacillation of 3-week period during the boreal winter season. Webster and Keller (1975) found a similar oscillation in the Southern Hemisphere (SH) stratosphere. These quasi-periodic 3- to 6-week variations are known as zonal index cycles (Namais 1950). The present study confirms these oscillations, as seen in cold cloud index in the extratropics of the SH (22.5°–31.5°S). In this area approximately 20-day oscillations are seen in the autumn and winter; however, their existence in the summer and spring at the scale level 7 is obscure. There also exist approximately 10-day oscillations during the same seasons, probably due to baroclinic waves similar to those observed by Randel and Stanford (1985). However, in this area the high-frequency oscillations (~5- and 1-day periods) are mainly due to convective cloudiness in the summer months.

Acknowledgments. The authors thank the two anonymous reviewers for their insightful comments and sug-

APPENDIX
Relationship between Scale and Periodicities for Wavenumbers $\omega_0 = 5.3364$ and $\omega_0 = 10.0$.

Scale	Periodicity			
	$\omega_0 = 5.3364$		$\omega_0 = 10.0$	
	3 h	Days	3 h	Days
2.0	4.63	0.58	2.50	0.31
2.1	4.96	0.62	2.68	0.34
2.2	5.32	0.67	2.87	0.36
2.3	5.70	0.71	3.08	0.39
2.4	6.11	0.76	3.30	0.41
2.5	6.55	0.82	3.54	0.44
2.6	7.02	0.88	3.79	0.47
2.7	7.52	0.94	4.06	0.51
2.8	8.06	1.01	4.36	0.54
2.9	8.64	1.08	4.67	0.58
3.0	9.26	1.16	5.00	0.63
3.1	9.93	1.24	5.36	0.67
3.2	10.64	1.33	5.75	0.72
3.3	11.40	1.43	6.16	0.77
3.4	12.22	1.53	6.60	0.83
3.5	13.10	1.64	7.08	0.88
3.6	14.04	1.76	7.58	0.95
3.7	15.05	1.88	8.13	1.02
3.8	16.13	2.02	8.71	1.09
3.9	17.29	2.16	9.34	1.17
4.0	18.53	2.32	10.01	1.25
4.1	19.86	2.48	10.73	1.34
4.2	21.28	2.66	11.50	1.44
4.3	22.81	2.85	12.32	1.54
4.4	24.45	3.06	13.20	1.65
4.5	26.20	3.28	14.15	1.77
4.6	28.08	3.51	15.17	1.90
4.7	30.10	3.76	16.26	2.03
4.8	32.26	4.03	17.42	2.18
4.9	34.57	4.32	18.67	2.33
5.0	37.05	4.63	20.01	2.50
5.1	39.71	4.96	21.45	2.68
5.2	42.56	5.32	22.99	2.87
5.3	45.62	5.70	24.64	3.08
5.4	48.89	6.11	26.41	3.30
5.5	52.40	6.55	28.30	3.54
5.6	56.16	7.02	30.34	3.79
5.7	60.19	7.52	32.51	4.06
5.8	64.51	8.06	34.85	4.36
5.9	69.14	8.64	37.35	4.67
6.0	74.11	9.26	40.03	5.00
6.1	79.42	9.93	42.90	5.36
6.2	85.13	10.64	45.98	5.75
6.3	91.24	11.40	49.28	6.16
6.4	97.78	12.22	52.82	6.60
6.5	104.80	13.10	56.61	7.08
6.6	112.32	14.04	60.67	7.58
6.7	120.39	15.05	65.03	8.13
6.8	129.03	16.13	69.70	8.71
6.9	138.29	17.29	74.70	9.34
7.0	148.21	18.53	80.06	10.01
7.1	158.85	19.86	85.80	10.73
7.2	170.25	21.28	91.96	11.50
7.3	182.47	22.81	98.56	12.32
7.4	195.57	24.45	105.64	13.20
7.5	209.60	26.20	113.22	14.15
7.6	224.65	28.08	121.35	15.17
7.7	240.77	30.10	130.06	16.26
7.8	258.05	32.26	139.39	17.42
7.9	276.57	34.57	149.39	18.67
8.0	296.42	37.05	160.12	20.01

getions, which improved the clarity of the text. SRC and GSSDP thank CNPq for the award of research fellowships.

REFERENCES

- Arkin, P. A., 1979: The relationship between fractional coverage of high cloud and rainfall accumulations during GATE over the B-scale array. *Mon. Wea. Rev.*, **107**, 1382–1387.
- Brier, G. W., and J. Simpson, 1969: Tropical cloudiness and rainfall related to pressure and tidal variations. *Quart. J. Roy. Meteor. Soc.*, **95**, 120–147.
- Chapa, S. R., and V. B. Rao, 1997: The diurnal, and semi-diurnal variations of convective activity in South America. Preprints, *Fifth Int. Conf. on Southern Hemisphere Meteorology and Oceanography*, Pretoria, South Africa, Amer. Meteor. Soc., 166–167.
- Chui, C. K., 1992: *An Introduction to Wavelets*. Academic Press, 226 pp.
- Ghil, M., and K. Mo, 1991: Intraseasonal oscillations in the global atmosphere. Part II: Southern Hemisphere. *J. Atmos. Sci.*, **48**, 780–790.
- Gray, W. M. and R. W. Jacobson Jr., 1977: Diurnal variations of oceanic deep cumulus convection. *Mon. Wea. Rev.*, **105**, 1171–1188.
- Grossmann, A., and J. Morlet, 1984: Decomposition of Hardy functions into square integrable wavelets of constant shape. *SIAM J. Math. Anal.* **15**, 723–736.
- Hsu, H.-H., 1996: Global view of the intraseasonal oscillation during northern winter. *J. Climate*, **9**, 2386–2406.
- , B. J. Hoskins, and F.-F. Jin, 1990: The 1985/86 intraseasonal oscillation and the role of the extratropics. *J. Atmos. Sci.*, **47**, 832–839.
- Knutson, T. R., and K. M. Weickmann, 1987: The 30–60-day atmospheric oscillations: Composite life cycles of convection and circulation anomalies. *Mon. Wea. Rev.*, **115**, 1407–1436.
- Kousky, V. E., 1988: Pentad outgoing longwave radiation climatology for the South American sector. *Rev. Bras. Meteor.*, **3**, 1951–1957.
- Kumar, P., and E. Foufoula-Georgiou, 1993a: A multicomponent decomposition of spatial rainfall fields: 1. Segregation of large- and small-scale features using wavelet transforms. *Water Resour. Res.*, **29**, 2515–2532.
- , and —, 1993b: A new look at rainfall fluctuations and scaling properties of spatial rainfall using orthogonal wavelets. *J. Appl. Meteor.*, **32**, 209–222.
- Lau, K.-M., L. Peng, C. H. Sui, and T. Nakazawa, 1989: Super cloud clusters, westerly wind burst, 30–60 day oscillations and ENSO: A unified view. *J. Meteor. Soc. Japan.*, **67**, 205–219.
- , T. Nakazawa, and C. H. Sui, 1991: Observations of cloud cluster hierarchies over the tropical western Pacific. *J. Geophys. Res.*, **96**, 3197–3208.
- Madden, R. A., and P. R. Julian, 1971: Detection of a 40–50 day oscillation in the zonal wind in the tropical Pacific. *J. Atmos. Sci.*, **28**, 702–708.
- McGuirk, J. P., and E. R. Reiter, 1976: A vacillation in atmospheric energy parameters. *J. Atmos. Sci.*, **33**, 2079–2093.
- Meisner, B. N., and P. A. Arkin, 1987: Spatial and annual variations in the diurnal cycle of large-scale tropical convective cloudiness and precipitation. *Mon. Wea. Rev.*, **115**, 2009–2032.
- Meyers, S. D., B. G. Kelly, and J. J. O'Brien, 1993: An introduction to wavelet analysis in oceanography and meteorology: With application to the dispersion of Yanai waves. *Mon. Wea. Rev.*, **121**, 2858–2866.
- Murakami, M., 1983: Analysis of deep convective activity over the western Pacific and southeast Asia. Part I: Diurnal variation. *J. Meteor. Soc. Japan*, **61**, 60–76.
- Nakazawa, T., 1988: Tropical super clusters within intraseasonal variations over the western Pacific. *J. Meteor. Soc. Japan*, **66**, 823–839.
- Namais, J., 1950: The index cycle and its role in the general circulation. *J. Meteor.*, **7**, 130–139.
- Nitta, T., and S. Sekine, 1994: Diurnal variation of convective activity over the tropical western Pacific. *J. Meteor. Soc. Japan*, **72**, 627–640.
- Pike, C. J., 1994: Analysis of high-resolution marine seismic data using the wavelet transform. *Wavelet Analysis and Its Applications*, Vol. 4, E. Foufoula-Georgiou and P. Kumar, Eds., Academic Press, 183–211.
- Randel, W., and J. L. Stanford, 1985: An observational study of medium-scale waves dynamics in the Southern Hemisphere summer. Part I: Waves structure and energetics. *J. Atmos. Sci.*, **42**, 1172–1188.
- Webster, P. J., and J. L. Keller, 1975: Atmospheric variations: Vacillations and index cycles. *J. Atmos. Sci.*, **32**, 1283–1300.
- Weng, H., and K.-M. Lau, 1994: Wavelets, period doubling, and time-frequency localization with application to organization of convection over the tropical western Pacific. *J. Atmos. Sci.*, **51**, 2523–2541.
- Yasunari, T., 1980: A quasi-stationary appearance of 30–40 day period in the cloudiness fluctuations during the summer monsoon over India. *J. Meteor. Soc. Japan*, **58**, 225–229.